Published in "Inorganic Chemistry 54(17): 8319–8326, 2015"
which should be cited to refer to this work.

Prospecting Lighting Applications with Ligand Field Tools and Density Functional Theory: A First-Principles Account of the $4f^7-4f^65d^1$ Luminescence of $CsMgBr_3:Eu^{2+}$

Harry Ramanantoanina,*[,†] Fanica Cimpoesu,*[,‡] Christian Göttel,[†] Mohammed Sahnoun,[§] Benjamin Herden,[†] Markus Suta,[∥] Claudia Wickleder,[∥] Werner Urland,*[,†] and Claude Daul*[,†]

[†]Department of Chemistry, University of Fribourg, Chemin du Musée 9, 1700 Fribourg, Switzerland

[‡]Institute of Physical Chemistry, Splaiul Independentei 202, Bucharest 060021, Romania

[§]Laboratoire de physique de la matière et modélisation mathématique LPQ3M, Université de Mascara, Mascara, Algerie

[∥]Faculty of Science and Technology, University of Siegen, Adolf-Reichwein Strasse 2, 57068 Siegen, Germany

ABSTRACT: The most efficient way to provide domestic lighting nowadays is by light-emitting diodes (LEDs) technology combined with phosphors shifting the blue and UV emission toward a desirable sunlight spectrum. A route in the quest for warm-white light goes toward the discovery and tuning of the lanthanide-based phosphors, a difficult task, in experimental and technical respects. A proper theoretical approach, which is also complicated at the conceptual level and in computing efforts, is however a profitable complement, offering valuable structure−property rationale as a guideline in the search of the best materials. The Eu^{2+}-based systems are the prototypes for ideal phosphors, exhibiting a wide range of visible light emission. Using the ligand field concepts in conjunction with density functional theory (DFT), conducted in nonroutine manner, we develop a nonempirical procedure to investigate the $4f^7-4f^65d^1$ luminescence of Eu^{2+} in the environment of arbitrary ligands, applied here on the $CsMgBr_3:Eu^{2+}$-doped material. Providing a salient methodology for the extraction of the relevant ligand field and related parameters from DFT calculations and encompassing the bottleneck of handling large matrices in a model Hamiltonian based on the whole set of 33 462 states, we obtained an excellent match with the experimental spectrum, from first-principles, without any fit or adjustment. This proves that the ligand field density functional theory methodology can be used in the assessment of new materials and rational property design.

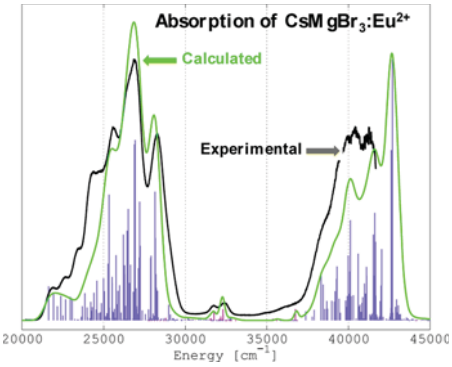

INTRODUCTION

The declaration, by the United Nations, of 2015 as the International Year of Light and Light-based Technologies[1] as well as the recent award of the Nobel Prize for the invention of efficient blue light-emitting diodes (LED), which has enabled bright and energy-saving white light sources,[2] put in sharp evidence the new impetus expected in such key domains, the energy saving turn of domestic lightening being one of the most immediate application goals. In the quest of finding phosphors able to alleviate the LED emission,[3] bringing it as close as possible to sun daylight or the so-called warm-white light[4−7] the systems based on lanthanide Eu^{2+}-doped active centers are among the best candidates.[4−7] Besides, the luminescence of Eu^{2+} compounds is interesting in academic respects, being a process essentially located at the atomic scale, due to the interconfiguration $4f^7-4f^65d^1$ transitions, which yield high quantum efficiency even at room temperature.[8−10] To complement the experimental efforts in the measurement the $4f^7-4f^65d^1$ excitation and the $4f^65d^1-4f^7$ emission spectra in various host materials, on the road of tuning proper compositions (host lattices and guest phosphors as doping), the theoretical branches can be called as the source of rationale for the red lines of property design.

The theoretical accounts of the electronic structure and the properties of Eu^{2+} considering its ground $4f^7$ and its first excited $4f^65d^1$ configurations are relatively rare. This is because the electronic structure of two-open-shell $4f^7$ and $4f^65d^1$ yields large matric interaction, namely, with 33 462 times 33 462 elements, generally prohibitive regarding computational cost. Therefore, the theoretical works are often tributary to standard ligand field theories fed by empirical parameters.[11−13] Most of the studies, phenomenological or first principles, have used the advent of high symmetry focusing primarily to the octahedral cases.[11−14] Nevertheless, the nature is more complicated than the preferred idealizations, the actual ongoing research[4−7,15−21] indicating the prevalence of systems where Eu^{2+} is in a lower coordination symmetry.

Herein we present a fully theoretical work based on density functional theory (DFT) enabling the investigation of the local structure of lanthanide-doped compounds, the calculation of

the electronic structure with respect to ligand field methodologies, and the prediction of the optical effects of the $4f^7-4f^65d^1$ transitions of Eu^{2+} embedded in the $CsMgBr_3$. This host compound crystallizes in the hexagonal $CsNiCl_3$ structure type with the space group $P6_3/mmc$ (no. 194),[22] giving rise to an intermediate symmetry case rather than the earlier octahedral situation. The lattice geometry of the $CsMgBr_3$ host is determined by means of DFT-based band structure calculations. However, the doping of Eu^{2+} into $CsMgBr_3$ and particularly the local distortion due to the presence of the Eu^{2+} impurity are explored by DFT geometry optimization operating with a selective cluster cut from the optimized $CsMgBr_3$ bulk. On the basis of charge balance, a primary supposition is that the Eu^{2+} impurity goes into the site formally occupied by the Mg^{2+} ion. Thus, the Eu^{2+} ion is coordinated by six bromide ligands forming a D_{3d} arrangement. The electronic structure of $(EuBr_6)^{4-}$ embedded in the $CsMgBr_3$ host is discussed with respect to ligand field analysis, showing the non-negligible influence of two Mg^{2+} ions capping the $(EuBr_6)^{4-}$ octahedron. The ligand field potential in the Wybourne parametrization is calculated together with the Slater–Condon integrals and the spin–orbit coupling constants. They are used to calculate the multiplet energy levels and the oscillator strength of the electric dipole moment of the interconfiguration $4f^7-4f^65d^1$ transitions. A priori, a special treatment of possible vibronic interaction in the $4f^7$ configuration has permitted the observation of some line intensities belonging to the intraconfiguration $4f^7-4f^7$ transitions, rendering therefore a realistic convoluted spectrum.

METHODOLOGY

The determination of the electronic structure of lanthanide-doped materials and the prediction of the optical properties are not trivial tasks. The standard ligand field models lack predictive power and undergoes parametric uncertainty at low symmetry, while customary computation methods, such as DFT, cannot be used in a routine manner for ligand field on lanthanide accounts. The ligand field density functional theory (LFDFT) algorithm[23−30] consists of a customized conduct of nonempirical DFT calculations, extracting reliable parameters that can be used in further numeric experiments, relevant for the prediction in luminescent materials science.[31] These series of parameters, which have to be determined in order to analyze the problem of two-open-shell 4f and 5d electrons in lanthanide materials, are as follows.

(1) The gap parameter $\Delta(fd)$, which represents the energy shift of the multiplets of the $4f^{n-1}5d^1$ configuration with respect to those of the $4f^n$. It is obtained as the difference in the barycenter of the DFT energies associated with the 30 030 Slater-determinants arising from the $4f^65d^1$ manifold and those 3432 from the $4f^7$.[23,32]

(2) The Slater–Condon integrals $F_k(ff)$, $F_k(fd)$, and $G_k(fd)$, which represent the static electron correlation within the $4f^n$ and $4f^{n-1}5d^1$ configurations. They are obtained from the radial wave functions R_{nl} of the 4f and 5d Kohn–Sham orbitals of the lanthanide ions.[23,31]

(3) The spin–orbit coupling constants ζ_{4f} and ζ_{5d}, which represent the relativistic spin–orbit interaction in the 4f and 5d shells, also determined by means of the radial wave functions R_{nl} of the 4f and 5d Kohn–Sham orbitals of the lanthanide ions.[23]

(4) The Wybourne crystal field parameters $B_q^k(f, f)$, $B_q^k(d, d)$, and $B_q^k(f, d)$, which describe the interaction due to the presence of the ligands onto the electrons of the lanthanide center. They are deduced from the ligand field energies and wave functions obtained from Kohn–Sham orbitals of restricted DFT calculations within the average of configuration (AOC) reference by placing evenly $n - 1$ electrons in the 4f orbitals and one electron in the 5d.[33]

The lattice geometry of $CsMgBr_3$ is approached via periodical calculations by means of the VASP program package.[34,35] The local density approximation (LDA) based on VWN[36] and the generalized gradient approximation (GGA) formulized in PBE[37] are used for the exchange and correlation functional. The interaction between valence and core electrons is emulated with the projected augmented wave method.[38,39] External as well as semicore states are included in the valence. A plane-wave basis set with a cutoff energy of 520 eV is used. Four k points were included in the direction a and b of the lattice, while 6 k points were comprised in the direction c.

The atomic positions were allowed to relax until all forces were smaller than 0.005 eV/Å. The local structure of the Eu^{2+} impurity in $CsMgBr_3$ is tackled via geometry optimization based on the cluster approach.[40] The optimized lattice structure of $CsMgBr_3$ is used. An appropriate cluster is obtained as a selective cut along the 3-fold c axis of the unit cell of $CsMgBr_3$ (Figure 1a). A moiety containing five units

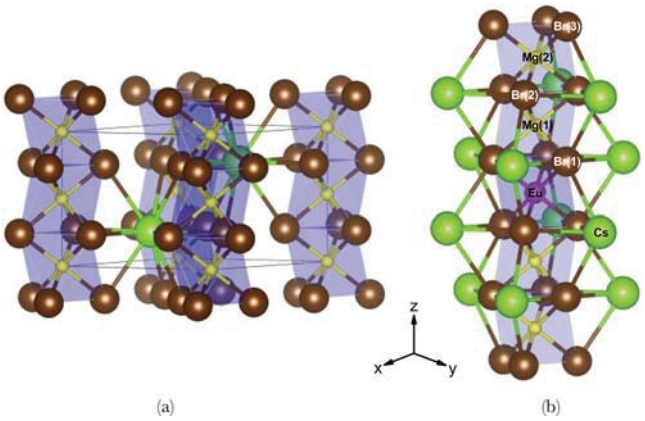

Figure 1. Representation of the crystal structure of $CsMgBr_3$ (a) and a selective cut along the z axis showing five units of face-sharing $(MgBr_6)^{4-}$ where the Eu^{2+} dopant is placed into the position of the central Mg^{2+} ion (b).

of face-sharing $(MgBr_6)^{4-}$ octahedra (Figure 1b) represents a perfect balance between the total number of atoms in the cluster (i.e., 35) and the charge of the edifice (i.e., + 4). This cluster is relaxed, keeping the electronic structure to have the $4f^7$ and $4f^65d^1$ electron configurations of Eu^{2+}, respectively. The positions of the atoms are relaxed, except those corresponding to Br(3), Mg(2), and their mirror images, as well as all Cs centers (Figure 1b), kept frozen to the optimized $CsMgBr_3$ bulk, to mimic the presence of the lattice. The DFT calculations have been carried out by means of the Amsterdam Density Functional (ADF) program package (ADF2013.01),[41−43] which is one of the few DFT codes having the set of keywords facilitating the AOC calculations and Slater-determinant emulation needed by the LFDFT algorithm.[23−33] The LDA VWN functional[36] as well as the GGA PBE functional[37] are used for the geometry optimization. The molecular orbitals are expanded using triple-ζ plus two polarization Slater-type orbital (STO) functions (TZ2P+) for the Eu atom and triple-ζ plus one polarization STO function (TZP) for the Cs, Mg, and Br atoms. The LFDFT modeling of the electronic structure and the related optical properties of $CsMgBr_3:Eu^{2+}$ is done using the hybrid B3LYP functional, in line with previous works.[23,30−33]

RESULTS AND DISCUSSION

Local Structure of the Eu^{2+} Impurity. From the experimental perspective, the doping of lanthanide ions into solid state materials can be probed by different instrumental technics such as nuclear magnetic resonance (NMR),[44] extended X-ray absorption fine structure (EXAFS),[45,46] or electron paramagnetic resonance (EPR),[47] which instead of giving a direct clue of the local geometry offers only data that can be corroborated to it. From the theoretical point of view,

the classical way is the simulation by periodical crystal supercell structure[23,31,32] with band structure methodologies which are, however, not useful in the further advancement toward ligand field modeling.[40] Alternatively, one may consider a sufficiently large cluster, carrying out geometry optimization by appropriate management of the variable versus frozen geometry coordinates. Using the same computational tools employed in the LFDFT account, this scheme has then inner consistency. In previous work[32] we probed that the cluster optimization leads to results similar to the bulk supercell approach. By means of band structure calculation, the optimized lattice parameters of the pristine $CsMgBr_3$ system are given in Table 1 compared with the experimentally available X-ray diffraction data.[48] We investigate the local structure around the Eu^{2+} impurity, which is incorporated in the matrix of $CsMgBr_3$ (Figure 1). We use the optimized structure of $CsMgBr_3$ obtained at the LDA and GGA levels of theory (Table 1). Cesium magnesium bromide ($CsMgBr_3$) crystallizes in the hexagonal $P6_3/mmc$ space group (no. 194).[22,48] The divalent Eu^{2+} ions enter into the sites formally occupied by Mg^{2+}. They are coordinated by six bromide ligands within the D_{3d} point group.

Table 1. Optimized Lattice Parameters *a*, *b*, *c* (in Angstroms) and α, β, γ (in degrees) of $CsMgBr_3$ Obtained at the LDA and GGA DFT Levels of Theory, Together with the Experimental X-ray Diffraction Data (exp.)

	LDA	GGA	exp.[a]
a	7.3342	7.8198	7.610
b	7.3342	7.8198	7.610
c	6.3240	6.6228	6.502
α	90.0	90.0	90.0
β	90.0	90.0	90.0
γ	120.0	120.0	120.0

[a]Taken from ref 48.

The geometry of the cluster represented in Figure 1b is then optimized. Theoretical results performed at two different levels of theory are collected in Table 2, compared with the reference structure of $CsMgBr_3$ deduced from the experimental data.[48] The cluster geometry optimization approach is used instead of the band structure algorithm in the investigation of the local structure of the Eu^{2+} impurity because this procedure yields appropriate structure with defined electron configuration.[40] The 4f orbitals of Eu^{2+} split into a_{1u}, a_{2u}, a_{2u}, e_u, and e_u irreducible representations (*irreps*) of the D_{3d} point group (see Figure 2). On the other hand, the 5d orbitals of Eu^{2+} form the basis of a_{1g}, e_g, and e_g *irreps* (see Figure 3). The ground configuration geometry GC (Table 2) is reached distributing evenly seven electrons in the 4f orbitals of Eu^{2+}. Then the excited configuration geometry EC (Table 2) is attained by the self-consistency of an even distribution of six electrons in the 7-fold 4f orbitals, altogether with one electron placed in the a_{1g} component of the 5d orbitals. The LDA geometry optimization renders a closer match to the pristine $CsMgBr_3$ reference than the GGA treatment (Table 2), i.e., it induces less perturbation in the pure lattice probably because the simpler approximation catches better the global bonding trends of the lattice.

Calculation of the Slater–Condon, spin–orbit coupling and ligand field parameters. The luminescence of $CsMgBr_3$:Eu^{2+} is crucially dependent on the local coordination geometry of the Eu^{2+} dopant. Besides, a geometry change occurs in the excited state $4f^65d^1$ (see Table 2), leading to shifts of lines in the emission spectrum as compared to the absorption (Stokes shift).[49] Apparently intriguing, the excitation leads to a shortening of the Eu–Br(1) bond length (Table 2) because, contrary to the usual situation where orbital promotion increases the antibonding, the fact is that the occupation of the 5d orbitals strengthens the binding. This is because the 4f shell, having a radius smaller than the lanthanide ion itself, does not contribute to the chemical bonding, which is mostly ionic and partly due to donation effects into the 5d virtuals.[40,50−52] A surge of 5d electron population, by excitation, enhances the radial extension and bonding propensity of these functions, leading to shrinkage of the coordination radii.[40] According to the LFDFT methodology,[23,30] series of DFT calculations and subsequent analyses provide the ligand field one-electron parameters, the spin–orbit coupling constants (mainly one-electron character), and the related Slater–Condon integrals (two-electron, Coulomb, and exchange effects), further used in the full modeling of the complex

Table 2. Optimized Local Structure Around the Eu^{2+} Impurity Embedded in $CsMgBr_3$ for the Ground $4f^7$ (GC) and Excited $4f^65d^1$ (EC) Electron Configurations of Eu^{2+} Obtained at the LDA and GGA DFT Levels of Theory[a]

	GC		EC		
	LDA	GGA	LDA	GGA	exp.[b]
Eu–Br(1)	2.8169	2.8607	2.7687	2.8189	2.6648
Eu–Mg(1)	3.3924	3.4161	3.3118	3.3287	3.2510
Eu–Br(2)	5.2453	5.3287	5.1867	5.2914	5.3140
Eu–Mg(2)[c]	6.3240	6.6230	6.3240	6.6230	6.5020
Eu–Br(3)[c]	8.1798	8.5480	8.1798	8.5480	8.3973
Mg(1)–Eu–Br(1)	51.46	52.15	53.99	54.56	52.41
Mg(1)–Eu–Br(2)	24.84	25.08	25.58	25.72	23.41
Mg(1)–Eu–Br(3)[c]	14.89	14.43	14.89	14.43	14.56

[a]Distances between the Eu^{2+} dopant (in Angstroms) and next nearest neighbors and bond angles Mg–Eu–Br (in degrees) (Figure 1b). [b]The experimental data represent the crystal structure of $CsMgBr_3$ taken from ref 48. [c]In the cluster geometry optimization approach, the coordinates of Mg(2) and Br(3) species are kept frozen to the band structure data.

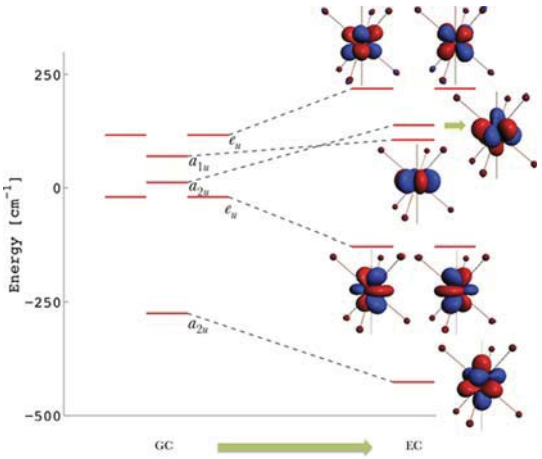

Figure 2. Representation of the energies of the 4f Kohn–Sham orbitals of Eu^{2+} in $CsMgBr_3$ obtained from the output of AOC-type calculation. The two diagrams represent the cases of geometries (Table 2) at ground and excited configurations (GC versus EC).

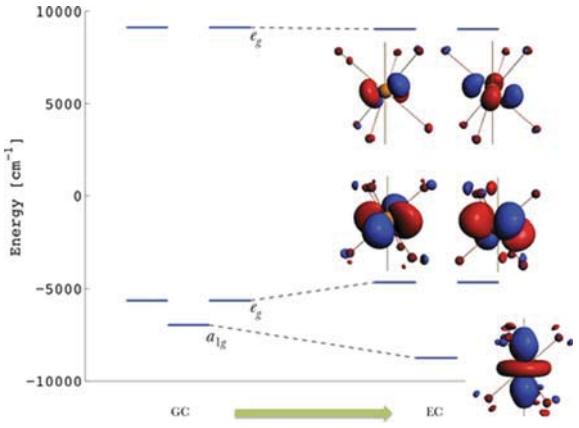

Figure 3. Representation of the energies of the 5d Kohn–Sham orbitals of Eu^{2+} in $CsMgBr_3$ obtained from the output of AOC-type calculation. The two diagrams represent the cases of geometries (Table 2) at ground and excited configurations (GC versus EC).

spectra.[53−55] In order to meet the premises of ligand field theory, the DFT calculations must be performed under the so-called average of configurations (AOC) calculation procedure.[23−33] It is a nonstandard handling that consists in imposing equal populations on the Kohn–Sham orbitals associated with the ligand field sequence, leading to a totally symmetric density. Then the orbital energies and eigenvectors are used to retrieve the ligand field matrix in atomic-like basis.[23−33] The spin–orbit coupling, bringing the relativistic effects together with the Slater–Condon integrals, is derived from the radial functions of the 4f and 5d Kohn–Sham orbitals of Eu^{2+} averaged in the bromide environment for both optimized structures in Table 2.[23,31] The calculated parameters are given in Table 3. The calculated ligand field parameters[33] of the 4f and 5d orbitals of Eu^{2+} are also shown in Table 3 as a function of the GC or the EC geometry (Table 2). The ligand field energies of the 4f and 5d orbitals of Eu^{2+} are graphically represented in Figures 2 and 3, respectively, as a function of the GC and EC geometries (Table 2).

The ligand field schemes are including the definite influence of the two Mg^{2+} ions capping the faces of the $(EuBr_6)^{4-}$ octahedron (Figure 1b). Their positive charges are exerting a stabilization trend against the electrons on the lanthanide, particularly for the orbitals pointing the lobes along the chain axis, i.e., fz^3 (Figure 2) and dz^2 (Figure 3) forming the basis of a_{2u} and a_{1g} representation in D_{3d}, respectively. Indeed, in the D_{3d} symmetry of the $(EuBr_6)^{4-}$ frame, the perturbation from the two apical Mg^{2+} neighbors (Figure 1b) spans the representation of a_{1g} and a_{2u} symmetry.

The former leads to the stabilization of same symmetry component in the 5d diagram (Figure 3), while the latter interacts with the a_{2u} from the 4f scheme (Figure 2). The ligand field energy parameters are larger in the excited states (Table 3) because of the previously mentioned enhanced bonding capabilities. The slight radial expansion of the occupied 5d orbitals, in comparison to their status as virtuals, enhances their interaction with the chemical environment.

Angular Overlap Model (AOM) Analysis of the Ligand Field Potential. For a gain of chemical intuition, we rewrite the ligand field potential in terms of the angular overlap model.[33] The site symmetry of the Eu^{2+} center is D_{3d}, and the ligand field splitting is mainly induced by the six equivalent Br(1) ligands as well as the two Mg(1) (Figure 1b). Therefore,

Table 3. Calculated Slater–Condon Integrals, Spin–Orbit Coupling Constants, and Ligand Field Parameters (in cm^{-1}) for $CsMgBr_3:Eu^{2+}$ Considering the Ground (GC) and Excited (EC) Configurations Local Structures of the Eu^{2+} Impurity

	GC	EC
$F_2(ff)$	388.47	388.47
$F_4(ff)$	49.92	49.92
$F_6(ff)$	5.30	5.30
$G_1(fd)$	124.52	116.17
$G_3(fd)$	11.00	8.64
$G_5(fd)$	1.72	1.28
$F_2(fd)$	87.01	76.12
$F_4(fd)$	6.48	4.85
$\Delta(fd)$	10 897.34	10 382.29
ζ_{4f}	1246.50	1246.50
ζ_{5d}	302.06	259.87
$B^2_0(f,f)$	−320.56	−723.85
$B^4_0(f,f)$	−475.07	−1194.36
$B^4_3(f,f)$	-*i*8.38	-*i*730.31
$B^4_{-3}(f,f)$	*i*8.38	*i*730.31
$B^6_0(f,f)$	−595.82	13.47
$B^6_3(f,f)$	-*i*291.33	-*i*152.72
$B^6_{-3}(f,f)$	*i*291.33	*i*152.72
$B^6_6(f,f)$	88.92	127.23
$B^6_{-6}(f,f)$	88.92	127.23
$B^2_0(d,d)$	125.18	−3419.09
$B^2_1(d,d)$	−22 267.87	−20 525.90
$B^2_{-1}(d,d)$	−22 267.87	−20 525.90
$B^4_0(d,d)$	−24 470.57	−28 082.92
$B^4_1(d,d)$	9090.82	8379.66
$B^4_{-1}(d,d)$	9090.82	8379.66

we can define the following set of parameters: $e_\sigma(f)_{Br^-}$, $e_\pi(f)_{Br^-}$, and $e_\sigma(f)_{Mg^{2+}}$ acting on the 4f orbitals and $e_\sigma(d)_{Br^-}$, $e_\pi(d)_{Br^-}$, and $e_\sigma(d)_{Mg^{2+}}$ acting on the 5d ones. The definition of the AOM parameters expresses the perturbation power of the environment sites on the σ and π interaction channels. The eigenvalues of the ligand field matrix, suggested in Figures 2 and 3, respectively for 4f and 5d orbitals, are used to obtain AOM parameters by least mean square fit. We calculated, for instance, in the case of the GC (Table 1) geometry the following parameters (in cm^{-1}), $e_\sigma(f)_{Br^-}$ = 109, $e_\pi(f)_{Br^-}$ = 92, $e_\sigma(f)_{Mg^{2+}}$ = −26, $e_\sigma(d)_{Br^-}$ = 8639, $e_\pi(d)_{Br^-}$ = 2900, and $e_\sigma(d)_{Mg^{2+}}$ = −1492, the mean deviations with the DFT results (Figures 2 and 3) being 7.39 and 0, respectively. The usual situation ranking of AOM parameters is $e_\sigma > |e_\pi|$ (occasionally with negative $|e_\pi|$ for the case of back-donation effects) and $|e_\lambda(d)| \gg |e_\lambda(f)|$ with $\lambda = \sigma,\pi$. Working with the nonstandard situation of accounting the perturbation from next neighbor cations, negative AOM parameters are obtained for the magnesium ions. This is perfectly reasonable considering that the positively charged sites must exert effects contrary to those emerging from the electron clouds of the ligands. One obtains a perfect mapping between the DFT results and the AOM formalism for the 5d ligand field. However, in the 4f block, the small deviation can be assigned as due to higher order perturbations.[33] The splitting of the 4f orbitals obtained from the DFT calculation is much smaller if compared to the 5d orbital spacing. Then the DFT calculation takes into consideration many quantum effects that might not be fully classified by the simple σ and π interactions of the AOM formalism. Also, the AOM gives an intuitive

description of the ligand field potential being here able to indicate the contribution of the two Mg^{2+} with negative e_σ values.

Multiplet Structure and Absorption Spectra. The calculated multiplet energy levels arising from the $4f^7$ and $4f^65d^1$ configurations of Eu^{2+} in $CsMgBr_3$ are presented in Figure 4 for the GC and EC geometries in Table 2. The $4f^7$

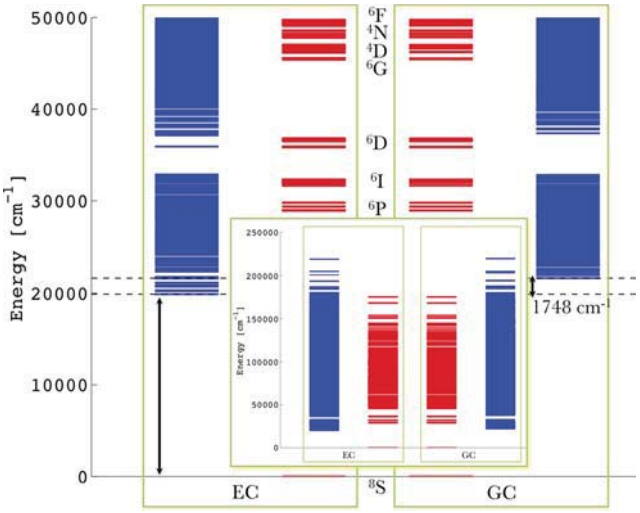

Figure 4. Calculated multiplet energy levels (zero-phonon lines) arising from the ground $4f^7$ (in red) and excited $4f^65d^1$ (in blue) configurations of Eu^{2+} in $CsMgBr_3$:Eu^{2+} obtained for the two geometries (LDA structures) representing the ground (GC) and excited (EC) configurations of Eu^{2+} (Table 2). The energy range from 0 to 50 000 cm^{-1} is selectively magnified showing the change in the $4f^65d^1$ energy levels of GC and EC. Some atomic spectral terms of the Eu^{2+} in the $4f^7$ configuration are given for clarity. All states, from spin octets to doublets, are included. (Inset) Full range spectrum.

obtains 3432 energy levels constituting 1716 Kramers doublets, while the $4f^65d^1$ leads to 30 030 states (15 015 Kramers-doublets). The $4f^7$ ground state, $^8S_{7/2}$, with a very small zero-field splitting is taken as the zero of the energy. The spectral energy levels of $4f^7$ (Figure 4, in red) are not significantly affected by the GC versus EC geometry change, contradictory to those of $4f^65d^1$ where a noticeable modification occurs (Figure 4). The computed Stokes shift is 1748 cm^{-1}, in the magnitude of the experimentally deduced value of 1920 cm^{-1}.[22] Considering the lowest margin of the $4f^65d^1$ manifold, a $4f^65d^1$–$4f^7$ emission at 19 885 cm^{-1} in the green spectral region (Figure 4) is predicted, also in agreement with the experimentally observed emission, i.e., 19 578 cm^{-1}[22]

The matrix element of the electric dipole moment operator $\vec{d}_\alpha$ is constructed in terms of the one-electron wave function ψ

$$\langle\psi_\mu|\vec{d}_\alpha|\psi_\nu\rangle = \frac{\sqrt{4\pi}}{3}\langle R_{n_\mu l_\mu}|r|R_{n_\nu l_\nu}\rangle\langle Y_{n_\mu l_\mu}|Y_{1,\alpha}|Y_{n_\nu l_\nu}\rangle \quad (1)$$

where in the right-hand side of eq 1 the term carrying the radial component is simple overlap integrals while the angular term is proportional with the Clebsh–Gordan coefficients.[53,56]

Considering μ, ν = 4f and 5d, eq 1 is a matrix with 12 by 12 elements, important for computation of the intensities of the transitions by distributing its elements over the whole manifold of the multielectron wave function. Considering the actual centrosymmetric D_{3d} coordination of Eu^{2+}, only the 7 by 5 elements corresponding to the off-diagonal $\langle\psi_{4f}|\vec{d}_\alpha|\psi_{5d}\rangle$ block are nonzero. Thus, in D_{3d} symmetry, the $4f^7 \rightarrow 4f^7$ transitions do not carry intensity. However, vibronic coupling can easily encompass the Laporte restriction because the complete wave function ψ must include electronic and vibrational parts

$$\psi_\mu = \psi_\mu^{\text{orbital}}\psi_\mu^{\text{vib}} \quad (2)$$

To demonstrate this mechanism, we break the D_{3d} symmetry of the complex. We have shown over the past two decades that multideterminantal DFT[57–59] is adequate to describe the vibronic interaction. Therefore, we reoptimize the geometry (LDA structure) corresponding to GC (Table 2) without any symmetry constraint (C_1), while previously we imposed the C_3 axis of the mother lattice. A tiny distortion from the D_{3d} symmetry occurred with about 0.0072 Å average bond length change and a shallow energy stabilization of 241 cm^{-1}. This affects by less than 5% the ligand field parameters, providing however a set of dipole moment integrals which (eq 1), taken in a relative sense, accounts for a weak intensity of the $4f^7 \rightarrow 4f^7$ transitions. This relaxation of the Born–Oppenheimer approximation is a convenient surrogate to describe the dynamic vibronic interaction

$$\langle\psi_{4f}^{\text{orbital}}\psi_{4f}^{\text{vib}}|\vec{d}_\alpha|\psi_{4f}^{\text{orbital}}\psi_{4f}^{\text{vib}}\rangle \neq 0 \quad (3)$$

that confers the intensity of the $4f^7 \rightarrow 4f^7$ transitions.

The $4f^7 \rightarrow 4f^65d^1$ transitions are electric dipole allowed, the intensity matrix elements being roughly the same in the D_{3d} and C_1 geometries.

Using the ligand field parameters, the two-electron integrals and spin–orbit coupling constants in Table 3 and the dipole matrix elements for the intensity part in eq 1, the prediction of the absorption spectrum is approached in Figure 5. One notes an exceptional match of the spectral profile of $CsMgBr_3$:Eu^{2+} [22] with the first-principles simulation of energies and intensities. The dominant intensity comes from the dipole-allowed $4f^7 \rightarrow 4f^65d^1$ transitions. Though small, the $4f^7 \rightarrow 4f^7$ part nicely accounts for the weak details visible as a distinct weak double peak placed at about 32 000 cm^{-1} in the canyon between the large bands and the soft slope at about 37 000 cm^{-1}, at the left margin of the second large band envelope (Figure 5).

The computed intensities of the predominant $4f^7 \rightarrow 4f^65d^1$ transitions, represented by the height of the lines, are well matching the resolution details of the complex experimental spectrum.[22] Note that unless there is a global scaling, because of the arbitrary units in experimental data, no fit is implied in the representation of computed results.

The strong line intensity laying at 43 000 cm^{-1}, while predicted, is not yet measured due to technical limits.[22] The virtue of LFDFT in retrieving realistic and detailed spectral data by first-principle route recommends the algorithm as a valuable complement in assessing various phosphor materials, along with experimental tests or by a priory property design, saving the tedious trial-and-error experimental combinatorial work.

Prediction of the Emission Spectrum. The prediction of the emission spectrum corresponding to the $4f^65d^1 \rightarrow 4f^7$ (^8S) transitions is rather delicate since the emission is the result of the relaxation from many states incorporating a humungous number of paths with nonradiative decay. By modest assumption, we can approximate the emission as the radiation from the lowest multiplet energy levels of the $4f^65d^1$ electron configuration (Figure 4) to the ground state of the $4f^7$, i.e., the $^8S_{7/2}$ that is further split by very small zero-field splitting. Then the electronic transition, which is electric dipole allowed, gives

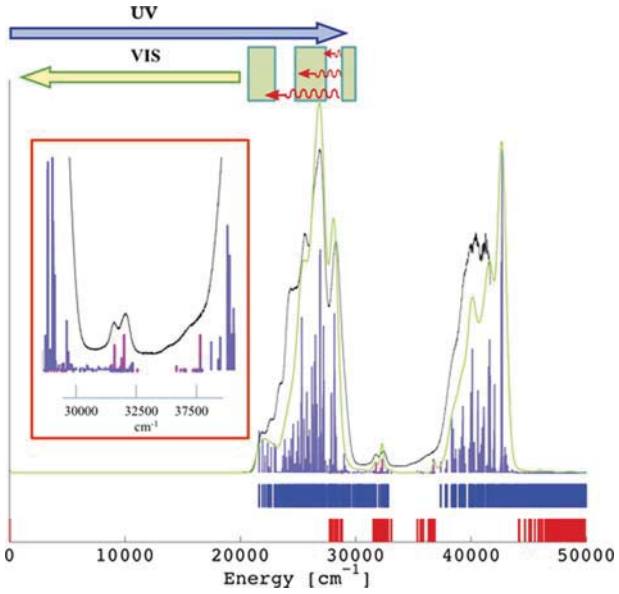

Figure 5. (Right) Calculated electric dipole oscillator strength (i.e., zero phonon lines) obtained for the transitions $4f^7$ (^8S) → $4f^65d^1$ (in violet) and $4f^7$ (^8S) → $4f^7$ (in magenta) of Eu^{2+} in $CsMgBr_3$:Eu^{2+} together with the experimental excitation spectra (in black) taken from ref 22. The multiplet energy levels corresponding to the $4f^7$ (in red) and $4f^65d^1$ (in blue) are presented on the bottom line. The green curve represents a superimposition of a Gaussian band with a width of 125 and 350 cm^{-1} on the zero phonon lines corresponding to the $4f^7$ (^8S) → $4f^7$ and $4f^7$ (^8S) → $4f^65d^1$ transitions, respectively. (Left-upper corner) Mechanisms of phosphor action, converting high-energy absorbed quanta to lower energy emission via arrays of nonradiative decay along the many states of the $4f^65d^1$ manifold comprised in the first band. (Left-side inset) Magnified sequence containing the $4f^7$ (^8S) → $4f^7$ weak intensity bands.

rise to one zero-phonon line emission, which is further coupled to vibrations. We use the so-called Huang–Rhys factor g_k[59−64] to measure the strength of the linear electron–phonon coupling. Since the transition path, which is used for the transformation of the EC geometry to the GC one (Table 2), conserves the D_{3d} symmetry, the Huang–Rhys factor are mainly associated with the totally symmetric vibrational mode a_{1g}. It is straightforward to consider the neutral cluster ($EuBr_6Mg_2$), whose coordinates are taken from Table 2, for the two stationary points GC and EC representing the structure of the Eu^{2+} impurity at the ground and excited configurations of Eu^{2+} in $CsMgBr_3$, respectively. The analytical harmonic frequencies and normal modes at the two stationary points are determined. They are presented in Table 4, where there are 21 normal modes belonging to the neutral cluster which form the basis of the following *irreps*: 3 a_{1g}, 3 e_g, a_{1u}, 3 a_{2u}, and 4 e_u (Table 4). The correlation between the normal modes of the GC and EC are constructed by means of the orthonormal Dushinsky matrix.[59,65] The displacement vector is the difference between EC and GC stationary points, and k expresses the contribution along the mass-weighted GC normal coordinates to the displacement vector. E_k represents the energy contribution of the normal modes on the relaxation of the EC stationary point to the GC one within the $4f^7$ electron configuration of Eu^{2+}.[59] They are also represented in Table 4. The Huang–Rhys factor g_k is related to k following ref 63.

The calculated values of the Huang–Rhys factor are also collected in Table 4, where it is seen that the contribution of

Table 4. Predicted Vibrational Energies $\hbar\omega$ (in cm^{-1}) Corresponding to the GC and EC Stationary Points, The Displacement Vector k (in ($amu^{1/2}$·Å)), the Energy Contribution E_k (in cm^{-1}), and the Huang–Rhys Factor g_k (dimensionless)

	$\hbar\omega$				
vib.	GC	EC	k	E_k	g_k
e_u	38.12	42.55	0.0000	0.00	0.00
a_{1u}	41.78	31.90	0.0000	0.00	0.00
a_{1g}	72.42	82.93	−3.0843	647.39	10.22
e_u	78.15	63.23	0.0000	0.00	0.00
e_g	83.39	62.44	−0.0017	0.00	0.00
a_{2u}	94.68	91.85	0.0000	0.00	0.00
e_g	137.70	147.54	−0.0013	0.00	0.00
a_{1g}	161.03	169.42	−0.4170	73.27	0.42
e_u	166.62	171.18	0.0000	0.00	0.00
a_{2u}	185.20	206.97	0.0000	0.00	0.00
e_u	214.64	214.82	0.0000	0.00	0.00
e_g	215.52	183.06	−0.0007	0.00	0.00
a_{1g}	267.28	262.71	−1.0481	137.61	4.35
a_{2u}	283.27	239.16	0.0000	0.00	0.00

the totally symmetric a_{1g} vibrational modes are the biggest, i.e., they are mainly responsible for the electron–phonon coupling. A graphical representation of their motion is given in Figure 6.

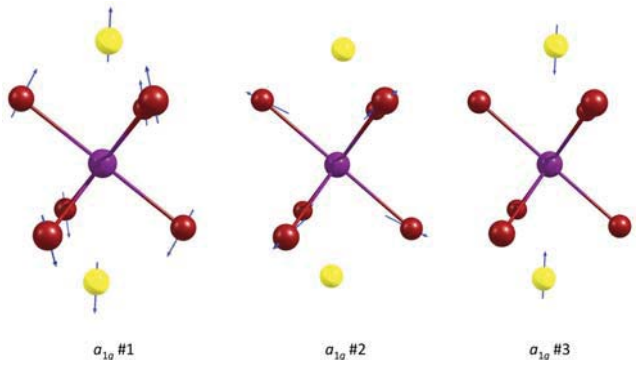

Figure 6. Representation of the three totally symmetric a_{1g} vibrations of ($EuBr_6Mg_2$) that is responsible of the electron phonon coupling in the $4f^65d^1$–$4f^7$ transitions of Eu^{2+} in $CsMgBr_3$. Color code: Eu^{2+} in violet, Br^- in red, and Mg^{2+} in yellow.

To simulate the vibrational progression, we obtain the Franck–Condon factors using the two-dimensional array method in ref 64. We consider 1 vibrational quantum (ν = 0) from the EC stationary point and 21 vibrational quanta (ν' = 0, 1, ..., 20) from the GC stationary point. The Franck–Condon factors are then calculated for every permutation up to 21 quanta over the vibrational modes. It is necessary in order to get all Franck–Condon factors of the EC stationary point with respect to each three a_{1g} vibrational state (Figure 6) of the GC to sum to one. One obtains a qualitative agreement between the calculated and the experimental emission profiles (Figure 7).

CONCLUSION

In this work, we outline the methodology for realistic analysis and first-principles prediction of the optical properties useful for obtaining phosphors, ameliorating the emission of LED devices by shifting the blue and UV predominance realizing

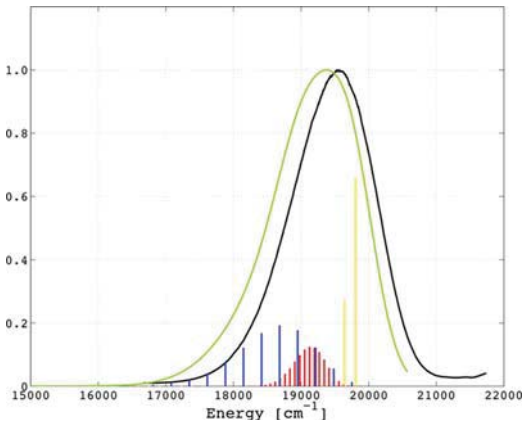

Figure 7. Calculated Franck–Condon factors of the EC stationary point with respect to the a_{1g} no. 1 (in red), a_{1g} no. 2 (in yellow), and a_{1g} no. 3 (in blue) vibrational states (Figure 6) of the GC stationary point. The green curve represents a superimposition of a Gaussian band with a width of 350 cm^{-1} on the Franck–Condon factors. The experimental observed emission spectrum[22] for the $4f^6 5d^1 \rightarrow 4f^7$ (^8S) transitions is given in black.

warm-white light. The LFDFT method consists of nonroutine DFT calculations setting numeric experiments defining the ligand field and related parameters (Slater–Condon integrals and spin–orbit coupling). Without the designed handling of spin and orbital population, the DFT in itself does not directly provide information consistent with the ligand field frame. The ligand field is a necessary ancillary tool, producing simulations of spectra, extending therefore the power of DFT, from where the parameters originate, beyond its nominal reach. The method was applied to $CsMgBr_3$ doped with Eu^{2+}, where a LFDFT modeling of $(EuBr_6)^{4-}$ octahedra belonging to an extended cluster mimicking well the local and long-range environment has been performed. The considered problem has a high level of technical difficulty in the ligand field modeling part, implying a nontrivial case of two-open-shell ligand field and a large dimension of Hamiltonian matrix, in general prohibitive, encompassed with special algorithmic steps of parallel computing. The match of experimental computed profiles to the experimental spectrum, in both major pattern and minor details, without adjustment or fit proves that the developed theoretical method is a reliable complement to experimental analysis.

AUTHOR INFORMATION

Corresponding Authors

*E-mail: harry.ra@hotmail.com.
*E-mail: cfanica@yahoo.com.
*E-mail: wurland@arcor.de.
*E-mail: claude.daul@unifr.ch.

Notes

The authors declare no competing financial interest.

ACKNOWLEDGMENTS

The Swiss National Science Foundation (SNF) and the Swiss State Secretariat for Innovation and Research supported this work. Funds from the UEFISCDI Romania research grant PCE 14/2013 are also acknowledged.

REFERENCES

(1) 2015 International year of light and light-based technologies, available http://www.light2015.org/Home.html [May 1, 2015].
(2) Heber, J. *Nat. Phys.* **2014**, *10*, 791.
(3) Nakamura, S.; Fasol, G. *The blue Laser Diode*; Springer: Berlin, 1997.
(4) Jüstel, T.; Nikol, H.; Ronda, C. *Angew. Chem., Int. Ed.* **1998**, *37*, 3084.
(5) Höppe, H. A. *Angew. Chem., Int. Ed.* **2009**, *48*, 3572.
(6) Bünzli, J.-C. G.; Piguet, C. *Chem. Soc. Rev.* **2005**, *34*, 1048.
(7) Eliseeva, S. V.; Bünzli, J.-C. G. *Chem. Soc. Rev.* **2010**, *39*, 189.
(8) Tyner, C. E.; Drickamer, H. G. *J. Chem. Phys.* **1977**, *67*, 4116.
(9) Kim, J. S.; Park, Y. H.; Kim, S. M.; Choi, J. C.; Park, H. L. *Solid State Commun.* **2005**, *133*, 445.
(10) Dorenbos, P. *J. Phys.: Condens. Matter* **2005**, *17*, 8103.
(11) Burdick, G. W.; Burdick, A.; Deev, V.; Duan, C.-K.; Reid, M. F. *J. Lumin.* **2006**, *118*, 205.
(12) Pan, Z.; Ning, L.; Cheng, B.-M.; Tanner, P. A. *Chem. Phys. Lett.* **2006**, *428*, 78.
(13) Garcia-Fuente, A.; Cimpoesu, F.; Ramanantoanina, H.; Herden, B.; Daul, C.; Suta, M.; Wickleder, C.; Urland, W. *Chem. Phys. Lett.* **2015**, *622*, 120.
(14) Aiga, F.; Hiramatsu, R.; Ishida, K. *J. Lumin.* **2014**, *145*, 951.
(15) Marchuk, A.; Schnick, W. *Angew. Chem., Int. Ed.* **2015**, *54*, 2383.
(16) Piao, X.; Machida, K.-I.; Horikawa, T.; Hanzawa, H.; Shimomura, Y.; Kijima, N. *Chem. Mater.* **2007**, *19*, 4592.
(17) Ruan, J.; Xie, R.-J.; Hirosaki, N.; Takeda, T. *J. Am. Ceram. Soc.* **2011**, *94*, 536.
(18) Xia, Z.; Zhang, Y.; Molokeev, M. S.; Atuchin, V. V. *J. Phys. Chem. C* **2013**, *117*, 20847.
(19) Bachmann, V.; Ronda, C.; Oeckler, O.; Schnick, W.; Meijerink, A. *Chem. Mater.* **2009**, *21*, 316.
(20) Krings, M.; Montana, G.; Dronskowski, R.; Wickleder, C. *Chem. Mater.* **2011**, *23*, 1694.
(21) Bachmann, V.; Jüstel, T.; Meijerink, A.; Ronda, C.; Schmidt, P. J. *J. Lumin.* **2006**, *121*, 441.
(22) Suta, M.; Larsen, P.; Lavoie-Cardinal, F.; Wickleder, C. *J. Lumin.* **2014**, *149*, 35.
(23) Ramanantoanina, H.; Sahnoun, M.; Barbiero, A.; Ferbinteanu, M.; Cimpoesu, F. *Phys. Chem. Chem. Phys.* **2015**, *17*, 18547.
(24) Atanasov, M.; Daul, C. A.; Rauzy, C. *Struct. Bonding (Berlin)* **2004**, *106*, 97.
(25) Atanasov, M.; Comba, P.; Daul, C. *J. Phys. Chem. A* **2006**, *110*, 13332.
(26) Atanasov, M.; Daul, C.; Gudel, H. U.; Wesolowski, T. A.; Zbiri, M. *Inorg. Chem.* **2005**, *44*, 2954.
(27) Atanasov, M.; Comba, P.; Daul, C. *Inorg. Chem.* **2008**, *47*, 2449.
(28) Atanansov, M.; Daul, C. *Chimia* **2005**, *59*, 504.
(29) Atanansov, M.; Daul, C. *C. R. Chim.* **2005**, *8*, 1421.
(30) Ramanantoanina, H.; Urland, W.; Cimpoesu, F.; Daul, C. *Phys. Chem. Chem. Phys.* **2013**, *15*, 13902.
(31) Ramanantoanina, H.; Urland, W.; Garcia-Fuente, A.; Cimpoesu, F.; Daul, C. *Phys. Chem. Chem. Phys.* **2014**, *16*, 14625.
(32) Ramanantoanina, H.; Urland, W.; Garcia-Fuente, A.; Cimpoesu, F.; Daul, C. *Chem. Phys. Lett.* **2013**, *588*, 260.
(33) Ramanantoanina, H.; Urland, W.; Cimpoesu, F.; Daul, C. *Phys. Chem. Chem. Phys.* **2014**, *16*, 12282.
(34) Kresse, G.; Hafner. *Phys. Rev. B: Condens. Matter Mater. Phys.* **1993**, *47*, 558.
(35) Kresse, G.; Furthmüller, J. *Phys. Rev. B: Condens. Matter Mater. Phys.* **1996**, *54*, 11169.
(36) Vosko, S. H.; Wilk, L.; Nussair, M. *Can. J. Phys.* **1980**, *58*, 1200.
(37) Perdew, J. P.; Burke, K.; Ernzerhof, M. *Phys. Rev. Lett.* **1996**, *77*, 3865.
(38) Blöchl, P. E. *Phys. Rev. B: Condens. Matter Mater. Phys.* **1994**, *50*, 17953.
(39) Kreese, G.; Joubert, D. *Phys. Rev. B: Condens. Matter Mater. Phys.* **1999**, *59*, 1758.

(40) Ramanantoanina, H.; Urland, W.; Herden, B.; Cimpoesu, B.; Daul, C. *Phys. Chem. Chem. Phys.* **2015**, *17*, 9116.
(41) te Velde, G.; Bickelhaupt, F. M.; van Gisbergen, S. J. A.; Guerra, C. F.; Baerends, E. J.; Snijders, J. G.; Ziegler, T. *J. Comput. Chem.* **2001**, *22*, 931.
(42) Guerra, C. F.; Snijders, J. G.; te Velde, G.; Baerends, E. J. *Theor. Chem. Acc.* **1998**, *99*, 391.
(43) Baerends, E. J.; Ziegler, T.; Autschbach, J.; Bashford, D.; Berces, A.; Bickelhaupt, F. M.; Bo, C.; Boerrigter, P. M. ; Cavallo, L.; Chong, D. P.; Deng, L.; Dickson, R. M.; Ellis, D. E.; van Faassen, M.; Fan, L.; Fischer, T. H.; Guerra, C. F.; Ghysels, A.; Giammona, A.; van Gisbergen, S. J. A.; Götz, A. W.; Groeneveld, J. A.; Gritsenko, O. V.; Grüning, M.; Gusarov, S.; Harris, F. E.; van den Hoek, P.; Jacob, C. R.; Jacobsen, H.; Jensen, L.; Kaminski, J. W.; van Kessel, G.; Koostra, F.; Kovalenko, A.; Krykunov, M. V.; van Lenthe, E.; McCormack, D. A.; Michalak, A.; Mitoraj, M.; Neugebauer, J.; Nicu, V. P. ; Noodleman, L.; Osinga, V.P.; Patchkovskii, S.; Philipsen, P. H. T.; Post, D.; Pye, C. C.; Ravenek, W.; Rodriguez, J. I.; Ros, P.; Shipper, P. R. T.; Schreckenbach, G.; Seldenthuis, J. S.; Seth, M.; Snijders, J. G.; Sola, M.; Swart, M.; Swerhone, D.; te Velde, G.; Vernooijs, P.; Versluis, L.; Vissher, L.; Visser, O.; Wang, F.; Wesolowski, T.; van Wezenbeek, E. M.; Wiesenekker, G.; Wolff, S. K.; Woo, T. K.; Yarkolev, A. L. *ADF2013.01*, available at http://www.scm.com.
(44) Walstedt, R. E.; Walker, L. R. *Phys. Rev. B* **1974**, *9*, 4857.
(45) O'Day, P. A.; Rehr, J. J.; Zabinsky, S. I.; Brown, G. E. *J. Am. Chem. Soc.* **1994**, *116*, 2938.
(46) Ghigna, P.; Carollo, A.; Flor, G.; Malavasi, L.; Peruga, G. S. *J. Phys. Chem. B* **2005**, *109*, 4365.
(47) Padlyak, B. V.; Grinberg, M.; Lukasiewicz, T.; Kisielewski, J.; Swirkowicz, M. *J. Alloys Compd.* **2003**, *361*, 6.
(48) McPherson, G. L.; McPherson, A. M.; Atwood, J. L. *J. Phys. Chem. Solids* **1980**, *41*, 495.
(49) Dorenbos, P. *J. Lumin.* **2000**, *91*, 155.
(50) Cimpoesu, F.; Dragoe, N.; Ramanantoanina, H.; Urland, W.; Daul, C. *Phys. Chem. Chem. Phys.* **2014**, *16*, 11337.
(51) Clark, D. L.; Gordon, J. C.; Hay, P. J.; Poli, R. *Organometallics* **2005**, *24*, 5747.
(52) Neidig, M. L.; Clark, D. L.; Martin, R. L. *Coord. Chem. Rev.* **2013**, *257*, 394.
(53) Griffith, J. S. *The theory of Transition Metal Ions*; Cambridge University Press: Cambridge, 1961.
(54) Figgis, B. N.; Hitchman, M. A. *Ligand field theory and its applications*; Wiley-VCH: New York, 2000.
(55) Gerloch, M.; Harding, J. H.; woodley, R. G. *Struct. Bonding (Berlin)* **1981**, *46*, 1.
(56) Cowan, R. D. *The theory of atomic structure and spectra*; University of California Press: Berkeley, 1981.
(57) Bruyndonckx, R.; Daul, C.; Manoharan, T. *Inorg. Chem.* **1997**, *36*, 4251.
(58) Ramanantoanina, H.; Gruden-Pavlovic, M.; Zlatar, M.; Daul, C. *Int. J. Quantum Chem.* **2013**, *113*, 802.
(59) Ramanantoanina, H.; Zlatar, M.; Garcia-Fernandez, P.; Daul, C.; Gruden-Pavlovic, M. *Phys. Chem. Chem. Phys.* **2013**, *15*, 1252.
(60) Wilson, E. B., Jr. *An Introduction to Scientific Research*; McGraw-Hill International Book Co., Inc.: New York, 1952.
(61) Balhausen, C. J. *Molecular Electronic Structure of Transition Metal Complexes*; McGraw-Hill International Book Co., Inc.: New York, 1979.
(62) Sharp, T. E.; Rosenstock, H. M. *J. Chem. Phys.* **1964**, *41*, 3453.
(63) Moreno, M.; Barriuso, M. T.; Aramburu, J. A. *J. Phys.: Condens. Matter* **1992**, *4*, 9481.
(64) Ruhoff, P. T.; Ratner, M. A. *Int. J. Quantum Chem.* **2000**, *77*, 383.
(65) Duschinsky, F. *Acta Physicochim. URSS* **1937**, *7*, 551−566.